

Laser diagnostics of pulverized coal combustion in O_2/N_2 and O_2/CO_2 conditions: velocity and scalar field measurements

Saravanan Balusamy¹  · M. Mustafa Kamal¹ · Steven M. Lowe¹ · Bo Tian¹ · Yi Gao¹ · Simone Hochgreb¹

Received: 21 November 2014 / Revised: 9 March 2015 / Accepted: 18 April 2015 / Published online: 13 May 2015
© The Author(s) 2015. This article is published with open access at Springerlink.com

Abstract Optical diagnostic techniques are applied to a 21 kW laboratory-scale pulverized coal–methane burner to map the reaction zone during combustion, in mixtures with varying fractions of O_2 , N_2 and CO_2 . Simultaneous Mie scatter and OH planar laser-induced fluorescence (PLIF) measurements have been carried out to study the effect of the oxidizer/diluent concentrations as well as the coal-loading rate. The spatial distribution of soot is captured using laser-induced incandescence (LII). Additionally, velocity profiles at selected axial locations are measured using the pairwise two-dimensional laser Doppler velocimetry technique. The OH PLIF images capture the reaction zones of pilot methane–air flames and the variation of the coal flame structure under various O_2/CO_2 compositions. Coal particles devolatilize immediately upon crossing the flame interface, so that the Mie scatter signal almost vanishes. Increasing coal-loading rates leads to higher reaction rates and shorter flames. LII measurements show that soot is formed primarily in the wake of remaining coal particles in the product regions. Finally, differences in the mean and RMS velocity field are explained by the combined action of thermal expansion and the changes in particle diameter between reacting and non-reacting flows.

1 Introduction

Coal-based thermal power plants provide almost 28 % of world's primary energy consumption and a 36 % of all CO_2

emissions (Metz et al. 2005; IEA 2012). Increasing demand for power, especially in developing countries, will lead to a further increase in CO_2 emissions and other harmful pollutants. To address the problem, several carbon capture and storage (CCS) technologies have been under development. One of the keys to CCS is the ability to increase CO_2 concentrations in the stream gas to make it economical for sequestration. Oxyfuel combustion, where oxygen diluted with exhaust CO_2 is used as an oxidizer rather than air, offers a possible way to achieve this. Several reviews have covered experimental and numerical modeling investigations of oxyfuel coal combustion technology (Buhre et al. 2005; Kurose et al. 2009; Wall et al. 2009; Toftgaard et al. 2010; Edge et al. 2011; Chen et al. 2012). Yet there are very few quantitative measurements detailing the flame structure of such turbulent oxygen-pulverized coal flames. A number of studies have used wavelength resolved optical emission in coal combustors to obtain total radiation, typically in the infrared region, as well as an estimate of particle temperatures by using the ratio of intensities at two different wavelengths (Saito et al. 1991; Murphy and Shaddix 2006; Zhang et al. 2010; Sung et al. 2011; Draper et al. 2012; Desmira et al. 2013). Measurements of the flame structure in pulverized coal are rarer, and even fewer measurements have been attempted under realistic flame configurations.

Previous measurements of pulverized coal flame structures include velocity measurements using laser Doppler velocimetry (LDV) (Pickett et al. 1999; Hwang et al. 2005, 2006a; Toporov et al. 2008; Balusamy et al. 2013), Mie scatter, OH planar laser-induced fluorescence (OH PLIF) and particle image velocimetry (PIV) by coal particles (Hwang et al. 2005, 2006a, b; Smith et al. 2002; Hayashi et al. 2013; Balusamy et al. 2013), as well as laser-induced incandescence (LII) by coal particles Hayashi et al. (2013). Most of the latter studies (Hwang et al. 2005, 2006a, b;

✉ Saravanan Balusamy
saravananb@iith.ac.in

¹ Department of Engineering, University of Cambridge,
Trumpington Street, Cambridge, UK

Hayashi et al. 2013) have been made in very small laboratory diffusion flames using methane as a carrier, which demonstrated the feasibility of the diagnostics and interpretation. Other studies (Smith et al. 2002) have used Mie scatter as a qualitative index for flame structure.

The present work is an advancement of the initial work carried out by Pickett et al. (1999), Hwang et al. (2005), Toporov et al. (2008) and Balusamy et al. (2013) to demonstrate how Mie scatter/OH PLIF, LDV and LII can be used in the study of the structure of swirling, turbulent, oxygen-enriched pulverized coal flames. Furthermore, this work identifies under which conditions OH PLIF and Mie scatter can be usefully employed in combination with LII to determine the extent of reaction, interpret the flame structure and heat release rate. Along the way, some of the pitfalls in such imaging measurements are identified, and possible alternatives to advance the measurements are suggested.

2 Experimental methodology

2.1 Laboratory-scale coal burner

Experiments are performed on an atmospheric, unconfined axisymmetric coal burner (Fig. 1). This burner has been used in previous studies, in which the flow field was characterized using LDV and PIV during the combustion of pulverized coal (Balusamy et al. 2013). The original burner design was modified to obtain higher overall reaction rates with the introduction of a central bluff body for flame stabilization (Fig. 1a). The resulting configuration consists of three coaxial tubes of 2 mm thickness, a swirler and a ceramic bluff body. Pulverized coal particles are transported to the central annulus of the burner by a mixture of metered gases. An outer pilot flame, consisting of a stoichiometric mixture of methane and air, is stabilized on the outer annulus above the axial swirler. A central flame, fueled by the incoming mixture of methane, coal, oxygen, and diluent nitrogen or carbon dioxide, is stabilized on the bluff body. The outer pilot flame and the inner coal–methane flame supply sufficient energy to ignite the coal particles and to support their reaction. A laminar co-flow stream is established in the outer annular region to isolate from external flow disturbances, providing well defined boundary conditions. The axial swirler consists of eight evenly spaced vanes of 1 mm thickness at an angle of 45° to the central axis. The swirl number, defined as the ratio of tangential to axial momentum, is estimated from the geometry (Kihm et al. 1990) as 0.77.

Figure 1b depicts the experimental setup of the coal burner. A screw feeder (K-Tron, K-MV-KT20 twin screw) is used to supply the pulverized coal particles to an eductor (Schutte and Koerting). The mass flow rate of coal is

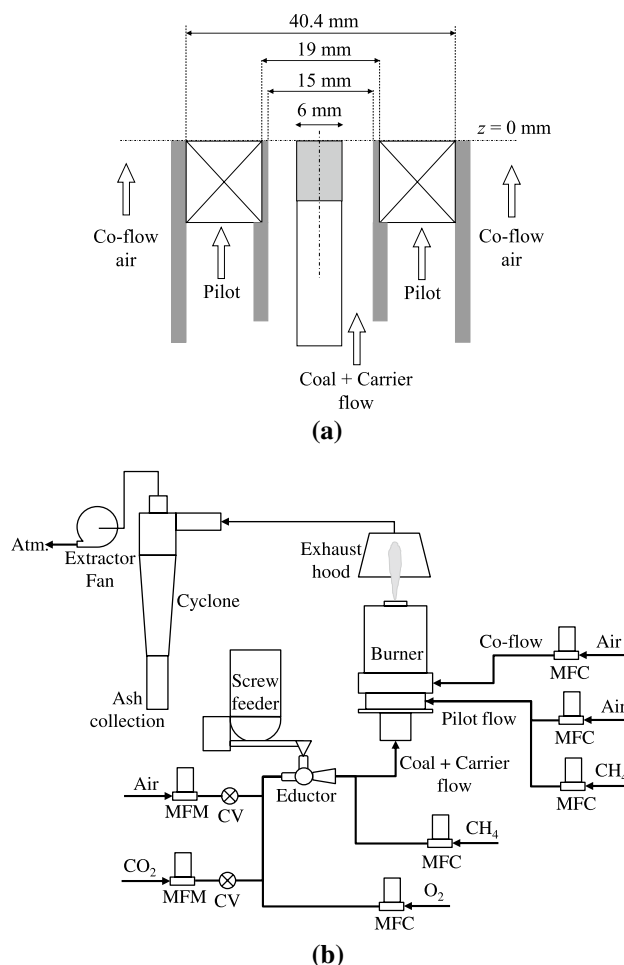


Fig. 1 Schematic diagram of coal burner setup. **a** Coal burner top section. **b** Flow configuration

metered by regulating the rotational speed of the DC motor driving the twin screws of the feeder. The carrier flow through the eductor entrains coal particles and transports them to the central annulus of the burner. The flow rates of the carrier air and CO₂ are metered individually through a mass flow meter (Alicat, M-100SLPM-D) using a fine-control needle valve. The flow rates of the carrier methane, carrier O₂, pilot air, pilot methane and co-flow air are regulated by mass flow controllers (Alicat MCR-D series) with an accuracy of ± 1.0 % of full scale. The unburned coal and ash particles are collected from the exhaust with the use of a cyclone, and the flue gas free of particles is released to the atmosphere.

The coal sample used in this study, obtained jointly by the EPSRC/EON Oxyfuel Network as representative of those used in UK power plants, originated from El Cerrejon, and its properties are given in Table 1. The particle size distribution obtained by sieving is shown on the table: Around 50 % of particles by mass are smaller than 75 μm , another 40 % are between 75 and 500 μm , and remainder

Table 1 Properties of El Cerrejon coal

Proximate analysis	wt%	
Volatile matter	34.80	
Fixed carbon	50.80	
Moisture	5.80	
Ash	8.60	
Ultimate analysis	wt%	
Carbon	69.20	
Hydrogen	4.40	
Oxygen	9.98	
Nitrogen	1.42	
Sulfur	0.58	
Sieve pitch (μm)	Cum. mass%	Mass%
500	100	10
210	90	28
150	62	12
75	50	22
<75	28	28
Lower heating value (MJ/kg)		27.12

are above $500\ \mu\text{m}$ in size. The particle relaxation time corresponding to the diameter of $75\ \mu\text{m}$ for a coal density of $640\ \text{kg/m}^3$ is around 10 ms, with an associated Stokes number of around 6, which clearly indicates that most of the particles may not follow the gas flow and turbulent fluctuations.

2.2 Test conditions

The test cases have been selected to study the effects of the (1) coal feeding rate for a fixed mass flow of oxidizer (2) O_2/CO_2 ratio. In all cases, the carrier gas volume flow rate is kept constant. This allows comparison of particle velocities under various test conditions for a fixed bulk velocity of carrier stream. The flow rates for the pilot and coflow streams are kept fixed for all cases, as given in Table 2. The coal feeding rate is varied by a factor of three for a fixed carrier gas composition (30 % $\text{O}_2/70\%$ N_2). The enrichment of oxygen in the carrier stream relative to air is essential to stabilize the coal flame on the bluff body. In Table 3, the carrier gas equivalence ratio ϕ_{CH_4} is calculated using the carrier gas composition excluding the coal supply. The bulk equivalence ratio is based on both coal and methane flow rates. The thermal input from the carrier methane flow ($0.5\ \text{m}^3/\text{h}$, $0.1\ \text{g/s}$) alone is around 4.9 kW. This additional heat input, together with the outer pilot flame, helps to ignite the pulverized coal particles supplied at ambient temperature in this open-type coal burner. The pilot conditions are kept stoichiometric, based on standard

Table 2 Flow conditions

Parameter	Carrier	Pilot	Coflow
Volume flow rate (m^3/h , STP ^a)	6.0	4.0	14.4
Mass flow rate (g/s)	1.9–2.6	1.25	4.74
Bulk equivalence ratio (–)	1.2–2.3	1.0	
Reynolds number (Re)	6200	1518	1944
Temperature (K)	293	293	293
Thermal input (kW)	4.9 ^b –17.4	3.4	

^a Standard temperature and pressure: 298 K and 101.32 kPa

^b The power from methane in the carrier flow is fixed at 4.9 kW

air (21 % $\text{O}_2/79\%$ N_2). To study the effect of O_2/CO_2 composition, three test cases (O1, O2 and O3) are gathered under constant coal mass flow rate with various gas compositions of the carrier flow. In those cases, the presence of N_2 (6 %, $0.3\ \text{m}^3/\text{h}$) is due to the ingress of air flow into the carrier stream through the screw feeder unit.

2.3 Optical diagnostic techniques

2.3.1 Laser Doppler velocimetry

Particle velocities are measured via the LDV technique. A dual-beam LDV system is utilized in the forward off-axis (30°) scattering configuration as shown in Fig. 2. The system consists of an Ar ion laser (Spectra-Physics Stabile 2017) operating with green (514.5 nm) and blue lines (488 nm) with a maximum power of 2 W, transmitted via fibers (Fibre-flow, Dantec) with a Bragg cell frequency shifter module on one of the beams to achieve directional sensitivity, and emitting through a 500 mm focal length lens to form the probe volume. The burst signal generated by the particles crossing the probe volume is collected through a Nikon Micro Nikkor 105 mm lens ($f/2.8$), a $100\ \mu\text{m}$ pin-hole, a photomultiplier outfitted with a color separator and a burst spectrum analyzer interfaced to a computer for the data processing. The photomultiplier is operated at 1600 V with signal gain of 24 dB. The minimum record length is set to 32 (number of samples of the shortest record length in auto-adaptive mode), and the maximum record length is set to 256 (number of samples of the longest record length in auto-adaptive mode). Level validation is fixed to 8 (ratio between the two highest peaks in the burst spectrum) for strict filtering. For each position, at least 2000 data points are obtained at a maximum data rate of 10 kHz. Axial and radial velocities (u and v) are measured with Configuration 1, in which the crossing vertical and horizontal planes are traversed along the centerline of the burner, perpendicular to the direction of beam propagation. The axial and tangential velocities (u and w) are measured with Configuration 2 as shown in Fig. 2, in which the vertical and horizontal

Table 3 Test matrix

Case	Flow rate coal mass (g/s)	Volume flow rate (m ³ /h, STP)	Composition (vol. %)	Carrier ϕ_{CH_4} (–)	Bulk ϕ (–)	Adiabatic flame temperature ^a (K)	
						Gas only	Gas + coal
A1	0.15	1.6/0.0/3.8/0.5	30/0/70	0.66	1.28	2095	2561
A2	0.31	1.6/0.0/3.8/0.5	30/0/70	0.66	1.97	2095	2097
A3	0.46	1.6/0.0/3.8/0.5	30/0/70	0.66	2.63	2095	1575
O1	0.46	1.6/3.5/0.3/0.5	30/64/6	0.66	2.63	1713	1269
O2	0.46	2.2/3.0/0.3/0.5	40/54/6	0.50	1.91	1738	2142
O3	0.46	2.5/2.7/0.3/0.5	45/49/6	0.44	1.68	1833	2516

^a Equilibrium calculations using the actual heating value and composition of coal, with thermodynamic properties from Kee et al. (1993)

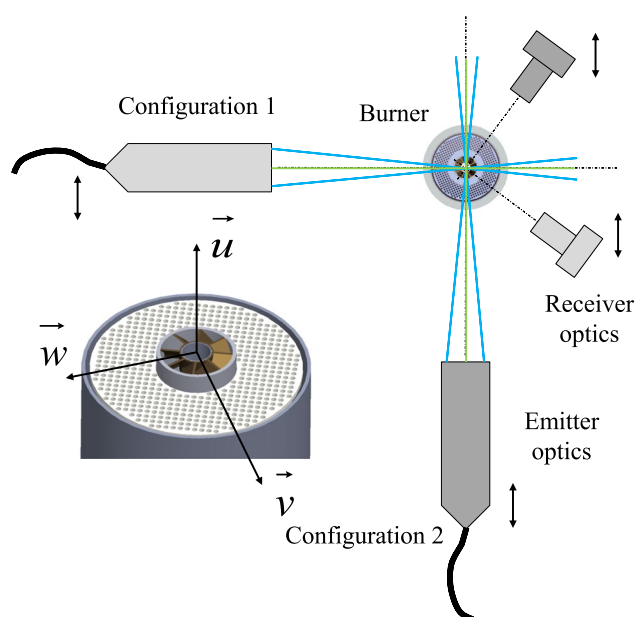


Fig. 2 Laser Doppler velocimetry (LDV) setup. Configuration 1 is shown in light gray color and Configuration 2 in dark gray color

planes are traversed along the centerline of the burner along the direction of the beams. The geometrical dimensions of the probe volume are $3.46 \times 0.14 \times 0.14 \text{ mm}^3$, which after factoring in the magnification of the lens, off-axis configuration and the pinhole in the receiver result in a probe volume of $0.91 \times 0.14 \times 0.13 \text{ mm}^3$.

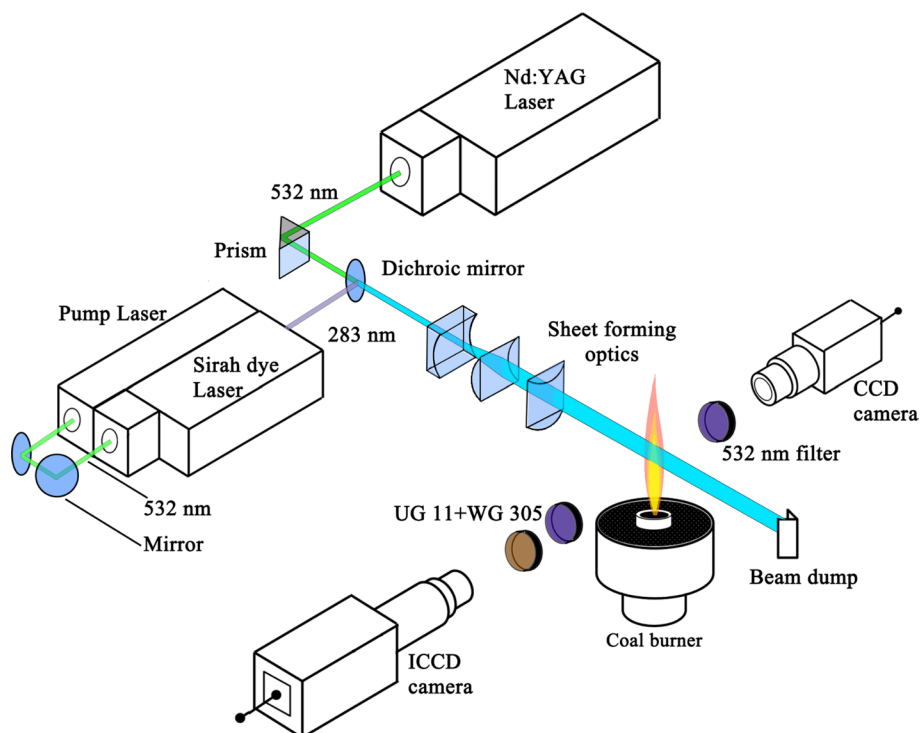
For measurements of the gas velocity, $1 \mu\text{m}$ calcined aluminum oxide (Al_2O_3), or alumina, is used as the seeder for all streams, including pilot and co-flow. For measurements with coal, the latter is used as the scattering particle in the carrier stream (no alumina particles), with other streams unchanged. This means that measurements are only possible while there are a sufficient number of particles in the flow. Once the coal particles devolatilize to a large extent in the product region, they no longer scatter, so that the data rate decreases, and measurements reflect a

concentration-weighted measure of velocity. The alumina particles are introduced into the flow streams by using fluidized bed generators. The seeding density is adjusted by regulating the bypass flow ratio, which is optimized to achieve maximum data rates.

2.3.2 Mie scatter/planar laser-induced fluorescence

The simultaneous measurement of Mie scatter and OH PLIF is realized by using the combined Mie/PLIF techniques as shown in Fig. 3. A Nd:YAG laser (Litron Nano PIV, 532 nm, 20 mJ/pulse) is used to illuminate the pulverized coal particles to generate Mie scatter. For the OH PLIF measurements, the transition of the $A^2\Sigma^+ - X^2\Pi(1, 0)$ band at 283.19 nm is excited, and fluorescence from the $A - X(1, 1)$, $(0, 0)$ and $B - X(0, 1)$ bands between 306 and 320 nm is detected. The PLIF laser system consists of a frequency-doubled Nd:YAG laser (Continuum, Surelite II, 532 nm, 300 mJ/pulse) and a tunable dye laser (Sirah CSTR-G-2400) with Rhodamine 6G dye in Ethanol solvent, and a second harmonic generator, which generates a UV beam of approximately 12 mJ pulse energy at 283.199 nm. The two laser beams (283.199 and 532 nm) are optically combined by a dichroic mirror, and the overlapped laser sheets are formed using a combination of spherical ($f = 500 \text{ mm}$) and cylindrical lenses ($f = 75 \text{ mm}$, $f = -25 \text{ mm}$, $f = 100 \text{ mm}$). The typical thicknesses of the visible and UV laser sheets at the imaging area are 800 and 500 μm , respectively. The Mie scatter signal from the coal particles is imaged using a CCD camera (LaVision Imager Pro X 4M, 1024×1024 pixels) equipped with a Nikon AF Micro Nikkor 60 mm lens ($f/4$) and a 50 mm interference filter (LOT-Oriel, center wavelength = 532 nm, half bandwidth = 9.42 nm, peak transmission = 64 %). The fluorescence from the excited OH radical is imaged onto the ICCD camera (LaVision Nanostar, gain 50 % and gate 100 ns, 512×512 pixels) fitted with a UV lens (Nikon, UV-Nikkor, 105 mm, $f/4.5$) and optical filters (Schott WG-305 and UG-11, about 55 % total transmissivity). The

Fig. 3 Combined setup of Mie scatter and OH PLIF technique



synchronization of laser units with cameras is realized using a programmable timing unit (PTU) from LaVision and a pulse delay generator (SRS, DG535). For each test point, 1000 Mie scatter and PLIF images are acquired at an acquisition rate of 10 Hz. All the images are postprocessed to account for the mean background noise and the spatial non-homogeneity of the laser sheet. The spatial resolution is about $59 \mu\text{m}/\text{pixel}$ for Mie scatter images and $121 \mu\text{m}/\text{pixel}$ for OH PLIF images.

2.3.3 Laser-induced incandescence

The LII technique is employed to measure the spatial distribution of the soot volume fraction of coal combustion. The LII setup is schematically depicted in Fig. 4. A Nd:YAG laser (Litron Nano PIV, 532 nm, 75 mJ/pulse) is used as illumination source. A laser sheet is formed using a combination of spherical ($f = 500 \text{ mm}$) and cylindrical lenses ($f = 75 \text{ mm}$, $f = -25 \text{ mm}$, $f = 100 \text{ mm}$). The imaging unit consists of a CCD camera (LaVision Imager Pro X 4M, 1024×1024 pixels) equipped with a gated intensifier (LaVision IRO, gain 75 % and gate 100 ns) and a Nikon AF Micro Nikkor 60 mm lens ($f/2.8$). The LII signal is collected at 430 nm through a band-pass filter (Thorlabs FB430-10, center wavelength = 430 nm, half bandwidth = 10 nm, peak transmission = 46 %). In order to avoid the signal emitted by the fluorescence of PAHs, the intensifier timing is delayed by 500 ns from the beginning of laser pulse. The laser sheet profile is obtained

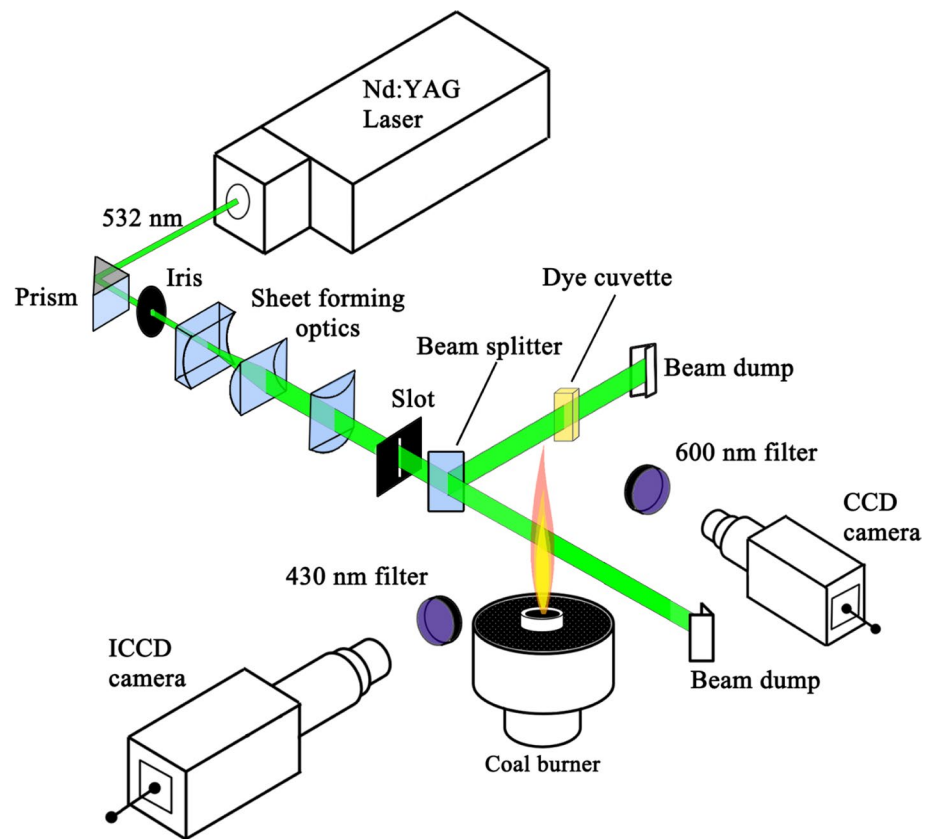
from the dye cuvette filled with Rhodamine 6G dye in ethanol solvent using a CCD camera (LaVision Imager Pro X 4M, 1024×1024 pixels) equipped with a Nikon AF Micro Nikkor 60 mm lens ($f/5.6$) and a band-pass filter centered at 600 nm. A slit is used to eliminate the low-energy regions of the laser sheet, and a homogeneous laser energy profile is obtained in the imaging area. The laser energy is optimized to achieve maximum LII signal intensity (Hayashi et al. 2013). The shot-to-shot variation of laser energy is $<2.5 \%$ of mean energy, which eliminates the shot-to-shot energy correction of LII images. For each test point, 2000 LII images are acquired at an acquisition rate of 10 Hz. All the images are postprocessed to eliminate the mean background noise. The spatial resolution of the LII images is about $64 \mu\text{m}/\text{pixel}$ and the imaging area is $65.8 \times 65.8 \text{ mm}^2$.

3 Results and discussion

3.1 Flame shape

Direct photographic images of pilot methane–air flame and pulverized coal flame for oxygen-enriched air and oxy-firing conditions are shown in Fig. 5. The exposure time is 20 ms (1/50) for gas-only flames and 0.25 ms (1/4000) for coal flames. The images with gas-only feeding show the inner lean flame produced by the carrier methane flow, stabilized on the bluff body lip and the inner tube rim, as well

Fig. 4 Laser-induced incandescence (LII) setup



as the swirl-stabilized outer stoichiometric pilot flame. We observe the effect of exchanging N_2 for CO_2 on the gas-only flame in Fig. 5b: for the lower intensity, colder inner flame is barely visible. This is consistent with a calculated change in equilibrium product temperature from 2095 K to 1713 K. The inner flame becomes shorter, with an increase of O_2 concentration in case (c). Figure 5d, e shows the effect of CO_2 on the coal flame. The very luminous coal flame under enriched air (d) becomes less reactive in case (e) when CO_2 is added. The enrichment of O_2 concentration in the carrier stream from 30 to 45 % increases the reaction rate in case (f), leading to higher radiative emissions. The effect of CO_2 on flame structure is examined in later subsections.

3.2 Mie scatter measurements

The Mie scatter measurements reveal the two-dimensional spatial distribution of particles. Figure 6 shows Mie scatter images for non-reacting flows (NRF) and reacting flows (RF). A higher resolution region of interest (ROI) is extracted from the centerline of images (a) and (b) to show the scatter in detail in (e) and (f), respectively. In the NRF case, the coal-laden flow shows the large-scale eddy structures of the inner flow mixing with the outer air, which are

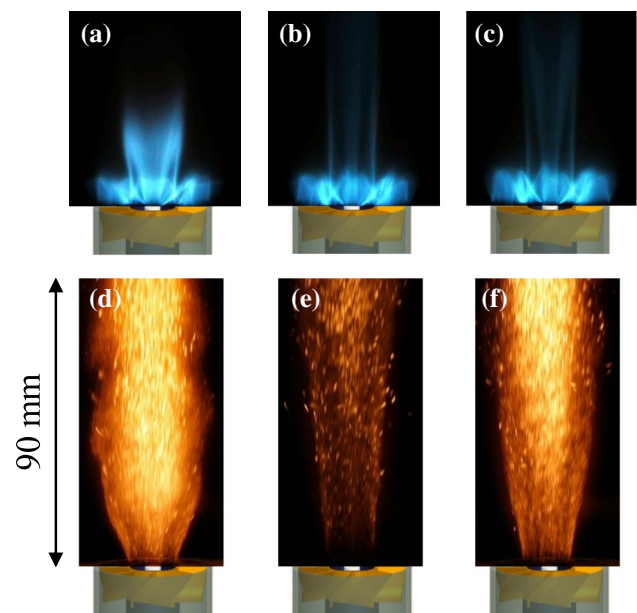
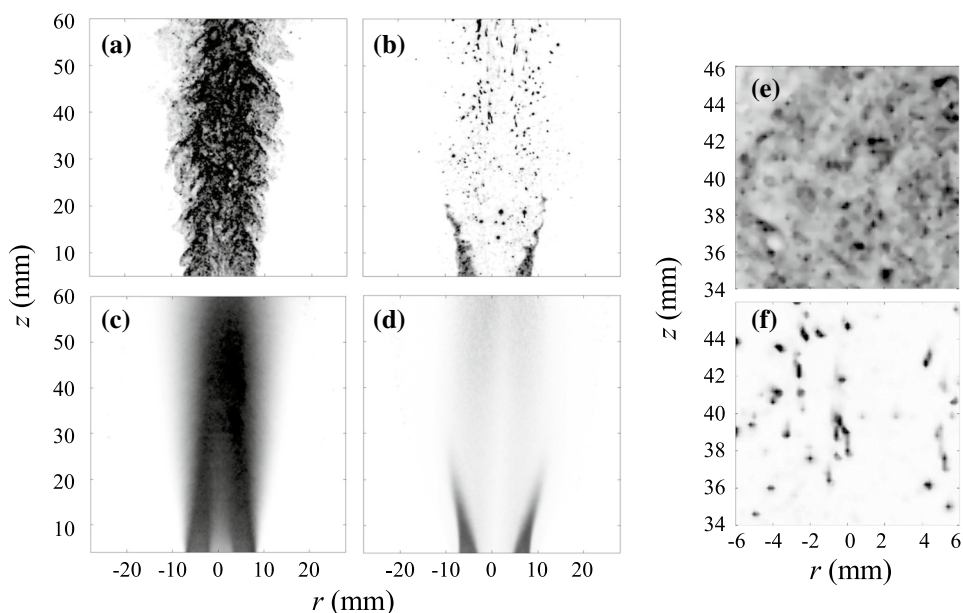


Fig. 5 Photographs of the flame with (a–c) gas only, and (d–f) gas + coal (coal mass flow rate = 0.46 g/s). Carrier flow composition: a, d 30 % O_2 /70 % N_2 , b, e 30 % O_2 /64 % CO_2 /6 % N_2 , c, f 45 % O_2 /49 % CO_2 /6 % N_2 . The yellow color is produced by the emission from coal and soot radiation

Fig. 6 Mie scatter images of pulverized coal particles (coal mass flow rate = 0.46 g/s). **a** Instantaneous non-reacting flow, **b** instantaneous reacting flow, **c** time-averaged non-reacting flow, **d** time-averaged reacting flow, **e** ROI of instantaneous NRF and **f** ROI of instantaneous RF. Images are normalized to the peak signal within the respective image sets



particularly visible along the shear layer between streams. In the non-reacting case, we observe significant nonuniformity shown in detail (e), which appears due to the range of coal particle sizes, with a baseline of alumina particles. The overall non-reacting mean image (c) shows the mixing along the outer shear layer and, interestingly, a lower intensity behind the bluff body. The latter is probably a result of the fact that only small particles follow the recirculation zone, with larger particles convected downstream. In contrast, the RF case (b) shows that the Mie signal largely disappears across the flame zone. There is intense Mie signal in the unreacted flow at the base, between the two branches of the outer pilot flame and the bluff body stabilized flame. The Mie signal cloud largely disappears across the flame zone, with the exception of isolated large spots, which sometimes appear as streaks. A detail of the reacting case just above the burner shows the presence of particles, with luminous wakes in their downstream region (f). The streaky spots emitting in this region arise from the luminosity generated by the localized combustion of the larger coal particles that have survived the flame—light is collected using a notch filter at 532 nm, which also collects a small amount of light from the broad flame luminescence around the particle wake. The wake arises due to the lower velocity of the particles relative to the surrounding flow (McLean et al. 1981; Prins et al. 1989). The time-averaged image in RF (d) shows that most of the particles do in fact disappear downstream of the flame, with a faint residue from burning particles and soot radiation emerging further down the flame zone. What is the reason behind the disappearance of the Mie scatter signal? Measurements of devolatilization of particles with a minimum 100 μm in initial diameter suggest devolatilization times of the order of

3–20 ms at temperatures around 1700 K, in various O_2 and CO_2 environments (Shaddix and Molina 2009). The work by Saito (1987) shows that oxidation of the remaining char is a much slower process, with oxidation times of the order of 200–300 ms at the same temperature. At the given bulk velocities of 5–10 m/s, the transit times through the flame are rather shorter, and full devolatilization of large particles could not happen within the sub-millisecond residence times across the flame zone. However, additional factors would contribute to the Mie signal disappearance: (a) the large number of smaller particles contributing to the signal, and the fact that the devolatilization time should depend on the square of the initial size of the particle, (b) the dependence of the Mie signal on the fourth power of the scattering particles, thus changing faster than the diameter itself, and (c) devolatilization changes the structure of the particle, so that one would expect increasingly less scatter and more transmission, possibly leaving networks of oxidizing char particles behind. This provides a rich source of gaseous hydrocarbons to react with the surrounding oxygen, increasing the local temperature and thus the mixture flame speed. Therefore, devolatilization is consistent with the observation of the sudden decrease in Mie scatter signal, as well as the shorter flame regions with increasing coal loading, which is discussed further on regarding the OH PLIF images.

Although the coal particles are nonspherical in shape, with wide size distribution and strong variation in particle density associated with coal particle devolatilization (Kalt et al. 2007), one can consider the relationship between the integrated Mie signal for the entire image for different coal-loading rates. The total Mie scatter signal increases linearly with the coal mass flow rate in both the RF and

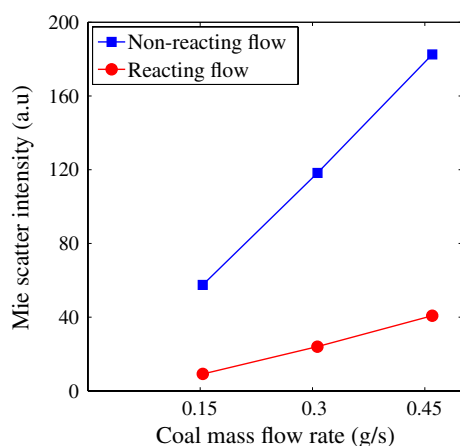


Fig. 7 Ensemble-averaged, integrated Mie scatter signals as a function of coal mass flow rates (30 % O₂/70 % N₂)

NRF cases as shown in Fig. 7. The difference in the total signal between reacting and non-reacting cases arises due to the disappearance of strongly scattering particles downstream of the main flame and should therefore be related to the rate of devolatilization and reaction of the original coal particles.

3.3 OH PLIF measurements of gas and coal flame

The OH PLIF images reveal the gas and coal flame structure for various gas compositions as shown in Fig. 8. In all cases, the OH PLIF signal is present in the burned gas region, peaking in the region of the outer pilot, as well as the inner pilot anchored on the central bluff body. The instantaneous images (left and middle column) show that the mean signal decreases from the right to the left side of the image, due to absorption of the UV light by the combustion gases. The images for the gas-only flames (left column) clearly show the boundaries between the unburned and burned gases.

Considering the gas-only left column, the flame length increases from the top row (a) (A3) to the middle row (b) (O3), as CO₂ is added to the inner mixture, and becomes longer as more CO₂ is added from the middle to the bottom row (c) (O1). The behavior of the gas-only OH PLIF is related to the overall equivalence ratios and consequent temperatures, which change from 2095 K for the top row (A3) to 1833 K for the middle row (O3), and drops further to 1713 K for the bottom row. Since this is an overall lean gas mixture, OH concentrations and reactivity increase with increasing the temperature, so that the flame length decreases as the O₂/CO₂ ratio increases from the bottom to the top row. Further, one can observe attenuation of the OH PLIF signal from right to left, which indicates absorption of laser light, as well as of the emitted signal by the flame

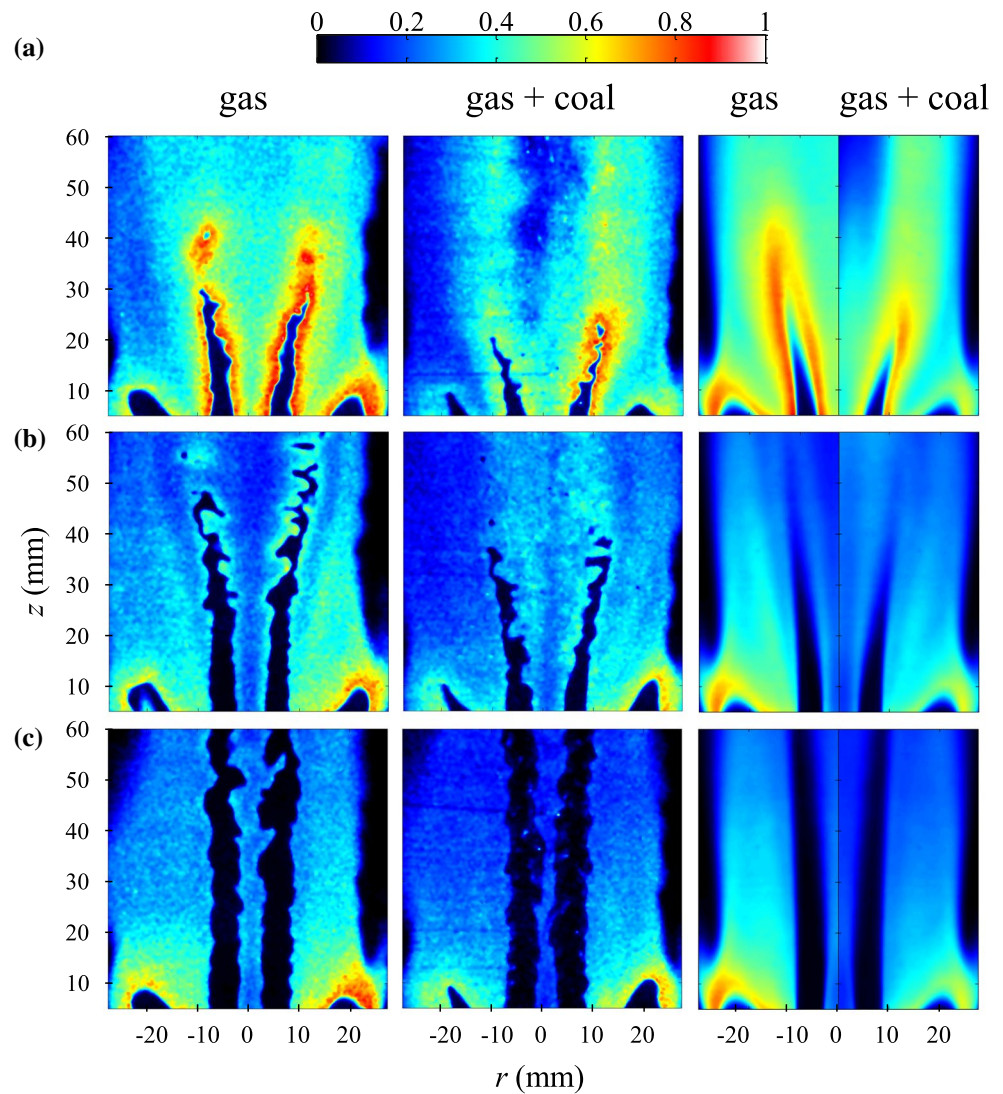
products (several species absorb in this range, particularly CO₂), so in the following discussion only the right-hand side of the images is considered.

The middle column shows the OH PLIF images for the corresponding combined gas and coal flames, and the right-most column shows averages of the right-hand half of all images, for gas and gas plus coal. Compared to the gas-only images on the left column, the coal–gas flame as marked by the OH PLIF interface is shorter for cases A3 (a) and O3 (b), which have higher temperatures than the O1 (c). As argued in connection with the Mie scatter images, the coal particles also act as a source of gaseous combustible hydrocarbons, which locally increase the gas phase equivalence ratio, contributing to the increase in flame speed and shortening the flame brush. The OH signal is somewhat lower in the coal-laden case (middle column) than the gas-only case (left column), particularly in case A3 (a). Given that OH concentrations in most hydrocarbon flames peak slightly in the slightly lean range, the addition of devolatilized hydrocarbons near the base of the flame pushes the equivalence ratio toward just over the stoichiometric and rich range (to about 1.2 assuming full oxidation of the 30 % of volatiles present), increasing the flame speed, but lowering OH concentrations, in agreement with the comparison between A3 with and without gas (top row). In addition, any CO from coal oxidation reactions should quickly react with OH, further depressing concentrations. At higher oxygen concentrations [case O3, middle row (b)], OH concentrations are also somewhat lowered relatively to the gas phase, but not as significantly as in the high CO₂/O₂ case O1 (c). For this last case O1, the already low OH signals for the gas-only flame are also lowered relatively to the baseline case. Although there is devolatilization and a slight narrowing of the inner flame relatively to the gas-only case, the overall OH PLIF signal is yet lower, which suggests further signal trapping by any additional CO₂ produced.

3.4 Simultaneous Mie and OH PLIF, and LII: effect of coal mass flow rate

Figure 9 shows the simultaneous instantaneous images of Mie/OH PLIF (left column) and randomly sampled, non-simultaneous instantaneous LII measurements (right column). The results are obtained for a fixed composition of carrier gas (30 % O₂/70 % N₂) and increasing loading rates of coal. The regions of high Mie scatter signal are in exact agreement with the unburned region as marked by the OH PLIF image. The overlap suggests that the coal particles, which provide the Mie scatter signal, devolatilize very fast as they cross the high-temperature flame region, so that there is little Mie signal from particles downstream of the flame. The hydrocarbons and other gases emerging from the devolatilized coal burn in the high-temperature region,

Fig. 8 Two-dimensional OH PLIF images for reacting flows. *Left column* instantaneous images for gas-only flame, *middle column* instantaneous images for gas + coal flame, *right column* time-averaged images of gas-only flame on left side and gas + coal flame on right side (coal mass flow rate = 0.46 g/s). **a** Case A3 (30 % O₂/70 % N₂), **b** O₃ (45 % O₂/49 % CO₂/6 % N₂) and **c** O₁ (30 % O₂/64 % CO₂/6 % N₂). All the images are normalized by the maximum intensity of gas-only flame (case A3)



contributing to the flame heat release, but not increasing the OH PLIF levels significantly. As discussed previously, this reflects the fact that the burning coal generates only low amounts of OH relative to the carrier gas mixture, owing to the low H/C ratio and overall rich conditions. The LII signal on the right-hand side column appears in the central product region. The LII signal arises from the instantaneous heating of particles to very high temperatures (around 4000 K) by the action of the laser energy. If the particles are as large as coal particles, the energy in the laser beam is insufficient to bring the particles to high temperatures, so no LII signal arises for the non-reacting flow condition. A test for interference was performed by collecting background images of reacting flows without the LII laser, which showed negligible interference from thermal emission and soot. This means that the signal arises from laser heating of small soot particles arising from the rich burning conditions downstream of the flame,

or possibly small unburned coal particles with similar properties.

As the coal loading increases from the top to the bottom row, the following features are observed: (1) The inner gaseous flame becomes shorter, but still overlaps with the inverse of each Mie scatter image, (2) an increased number of individual Mie scatter particles appear downstream of the flame interface, (3) an increase in LII signal intensity, a higher population of soot regions, and the appearance of streaky spots and (4) a decrease in OH PLIF intensity along the central region. The shorter flame region can be explained by the increased energy loading and higher temperatures, as explained above. The increased number of Mie scatter particles downstream of the flame arises both from the incomplete volatilization of coal particles and from increased amounts of soot formed. The increase in LII signal intensity and frequency confirms the presence of sooty particles. The discrete streaky spots in LII and Mie

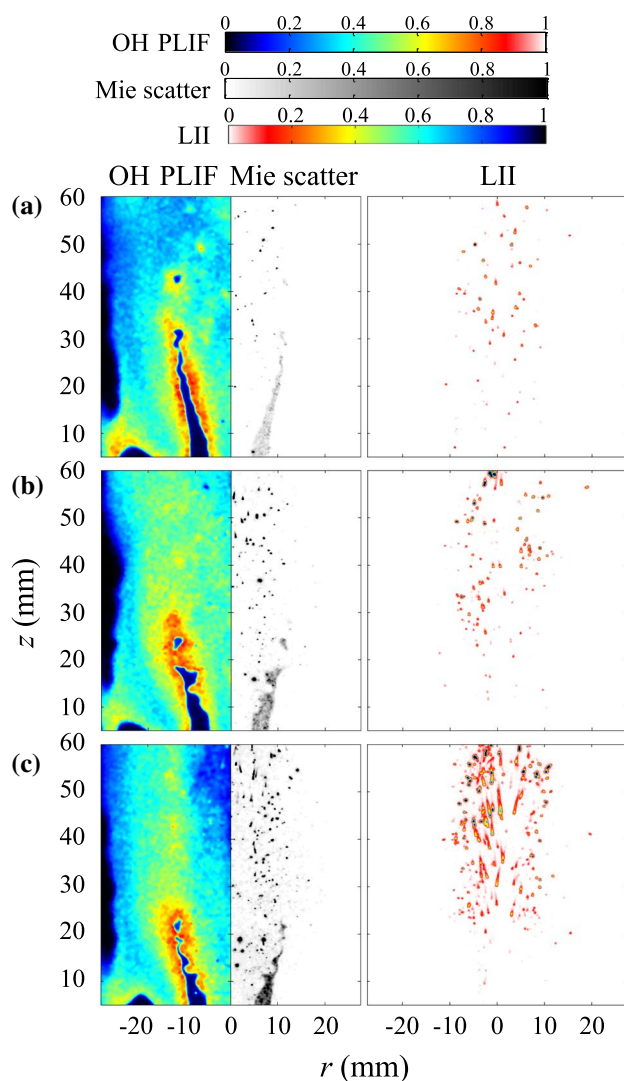


Fig. 9 Instantaneous two-dimensional images taken for reacting flows (30 % O₂/70 % N₂). *Left column* simultaneous Mie/OH PLIF images, *right column* LII images. **a** Coal mass flow rate = 0.15 g/s (case A1), **b** 0.31 g/s (A2) and **c** 0.46 g/s (A3). OH PLIF images are normalized by the maximum intensity of gas-only flame (case A3). Mie scatter images are normalized by the maximum intensity of case A3. LII images are normalized by the maximum intensity of ICCD camera

images do not arise from a time exposure of the camera, as this is very short (100 ns), but rather from the LII signal marking soot formation in the wake of burning coal particles. The wake arises because the solid particles move slower than the mean gas flow surrounding them.

The corresponding time-averaged images are shown in Fig. 10. The observations made about the instantaneous images are confirmed by the mean images. The gas expansion in the radial direction is observed with an increase in the coal feeding rate. Given that the gaseous carrier is

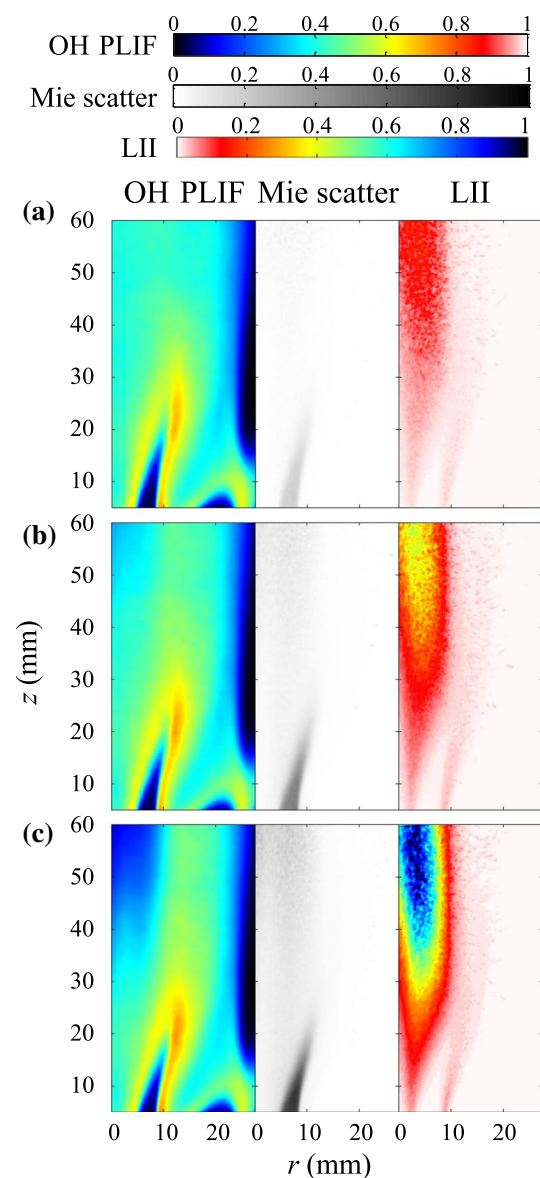


Fig. 10 Time-averaged two-dimensional images taken for reacting flows (30 % O₂/70 % N₂). *Left side* simultaneous Mie/OH PLIF images, *right side* LII images. **a** Coal mass flow rate = 0.15 g/s (case A1), **b** 0.31 g/s (A2) and **c** 0.46 g/s (A3). OH PLIF images are normalized by the maximum intensity of gas-only flame (case A3). Mie scatter images are normalized by the maximum intensity of case A3. LII images are normalized by the maximum intensity of case A3

unchanged, the gas expansion and the increase in LII signal reflect the fact that the coal heat release is contributing to the rise in the local flame temperature and thus to a faster turbulent flame. In the case of the highest coal loading (case A3), the OH PLIF signal disappears near the center of the flame where the Mie signal reappears, and the LII signal reaches a maximum intensity. The presence of Mie signal together with the absence of OH PLIF signal, combined

with the high-intensity LII signal in this region, reflects the lack of oxygen in these globally rich mixture conditions ($\phi_{\text{bulk}} = 2.3$) and consumption of any remaining oxygen by the devolatilized hydrocarbons and coal particles breaking through the main flame. As observed before (Hayashi et al. 2013), the low concentration of oxygen and the high temperatures enhance soot formation greatly. This is also reflected in the increased Mie scatter from soot particles in the center of the product region further downstream at high coal-loading rates.

3.5 Simultaneous Mie and OH PLIF, and LII: effect of O_2/CO_2 ratio

The effect of O_2/CO_2 ratio is studied under a fixed coal feeding rate (0.46 g/s). Figure 11 shows instantaneous images of Mie/OH PLIF and LII measurements taken for various carrier gas compositions, shown on the same intensity scale as Fig. 9. The spatial distribution of the fresh coal particles in the Mie scatter image is again in exact agreement with the unburned region as marked by OH PLIF image, and the LII images show a much lower soot formation in the oxy-firing cases in comparison with the enriched air-firing cases. As observed previously in Fig. 8 for OH PLIF, the flame becomes comparatively very long and narrow when the temperatures are lowered by CO_2 addition, but the features of the Mie scatter images are represented almost exactly as a negative of the OH images, showing that even at the lower temperatures, the particles devolatilize to a large extent. However, the observations point out that as the temperature decreases at this high coal loading (top and middle row, compared to bottom row), a larger fraction of the particles escapes devolatilization into the product region. However, the LII shows little soot formation under these conditions of comparatively high coal loading and low temperatures. The temperatures and oxygen concentrations become too low for soot formation, so only little LII signal is obtained downstream.

The time-averaged images further confirm the above observations as shown in Fig. 12. The mean LII images reveal some additional features: the concentration of soot particles appears higher near the outer pilot flame compared to the inner zone, but those concentrations decrease as the O_2 concentrations increase. This can be explained by the fact that the adiabatic temperatures of the outer pilot flame (2223 K) are significantly higher than the inner regions (1713 K) when CO_2 concentrations are high, so that more soot forms in the higher temperature regions near the interface of the outer pilot. As the O_2 concentrations increase further on the core inner flame, the temperatures and O_2 concentrations increase, promoting more soot formation in the inner product zone.

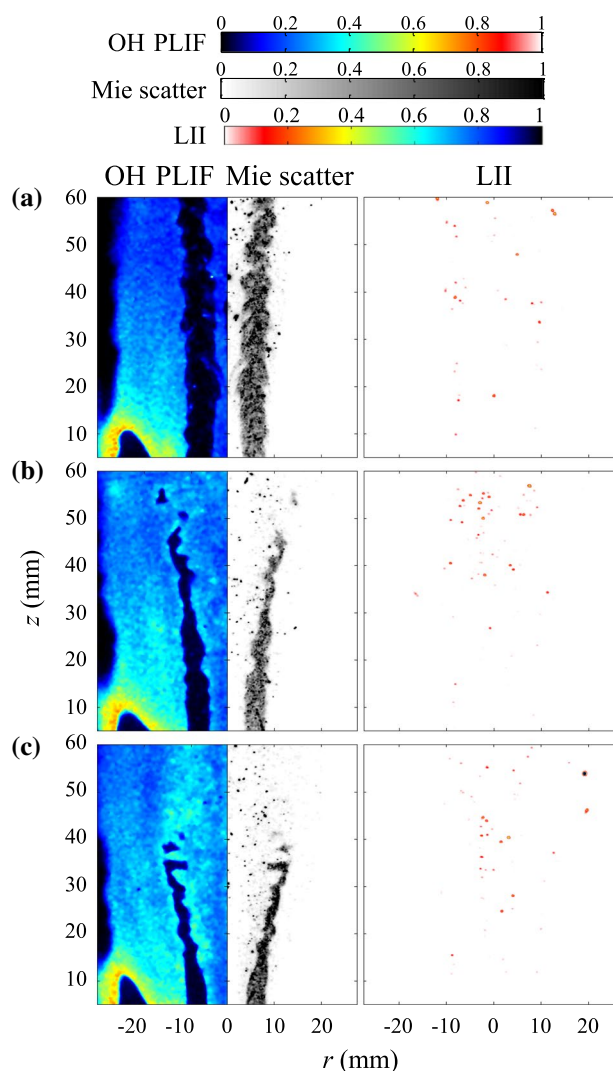


Fig. 11 Instantaneous two-dimensional images taken for reacting flows (coal mass flow rate = 0.46 g/s). *Left side* simultaneous Mie/OH PLIF images, *right side* LII images. **a** Case O1 (30 % O_2 /64 % CO_2 /6 % N_2), **b** O2 (40 % O_2 /54 % CO_2 /6 % N_2) and **c** O3 (45 % O_2 /49 % CO_2 /6 % N_2). OH PLIF images are normalized by the maximum intensity of gas-only flame (case A3). Mie scatter images are normalized by the maximum intensity of case A3. LII images are normalized by the maximum intensity of ICCD camera

3.6 Velocity measurements

Quantitative velocity measurements of the flow field have been produced in order to provide appropriate boundary conditions and data for comparison with CFD models. Measurements for both non-reacting and reacting conditions were made, at distances 2, 10, 20 and 30 mm from the burner inlet. In most cases, the coal particles start to disappear above $z = 30$ mm, so the measurements are restricted to be within 30 mm from the burner face, in order to collect sufficient signal from coal particles. Since Mie scatter signals from small particles are lower, the LDV measurements

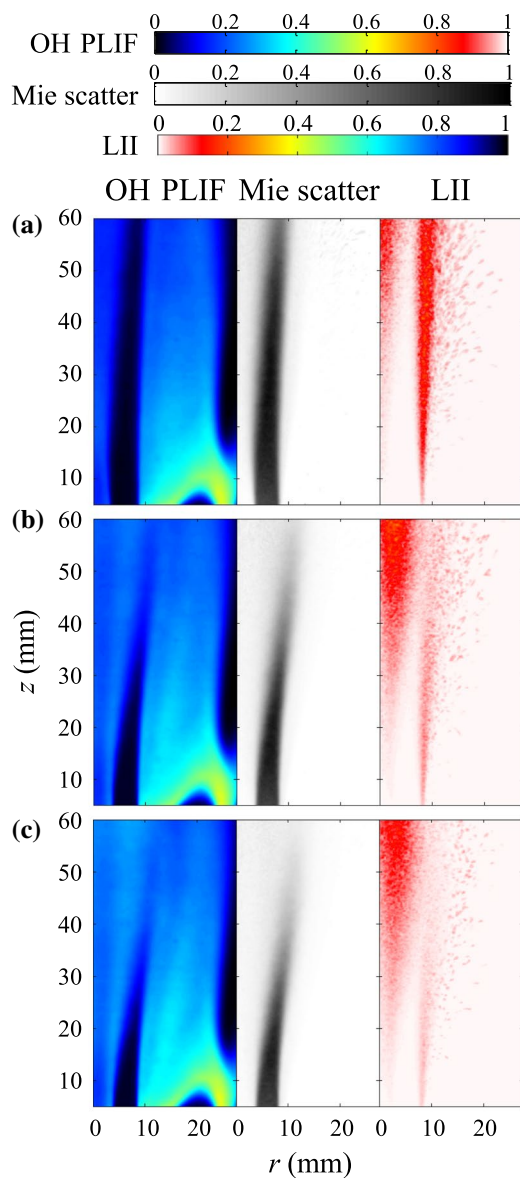


Fig. 12 Time-averaged two-dimensional images taken for reacting flows (coal mass flow rate = 0.46 g/s). *Left side* simultaneous Mie/OH PLIF images, *right side* LII images. **a** Case O1 (30 % O₂/64 % CO₂/6 % N₂), **b** O2 (40 % O₂/54 % CO₂/6 % N₂) and **c** O3 (45 % O₂/49 % CO₂/6 % N₂). OH PLIF images are normalized by the maximum intensity of gas-only flame (case A3). Mie scatter images are normalized by the maximum intensity of case A3. LII images are normalized by the maximum intensity of case A3

will arise from the small number of small particles surviving devolatilization, in a particle-weighted average. The gas phase velocities on the outer zone are obtained by LDV measurements by seeding alumina into the outer pilot, as well as into the inner region when no coal was employed. The coal particles act as scatterers for the coal and gas velocities, and represent the velocity of the lighter fractions of the coal particles (Balusamy et al. 2013). Two

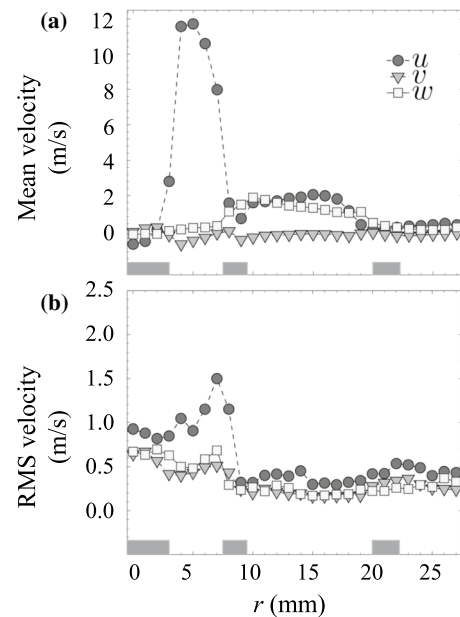


Fig. 13 Radial distribution of velocity components of coal particles measured at $z = 2$ mm by LDV technique for non-reacting flow condition (coal mass flow rate = 0.46 g/s). **a** Mean velocities, **b** RMS velocities

components of the velocity are obtained at a time, providing measurements of the three velocity components.

The radial distribution of mean and RMS velocities of axial (u), radial (v) and tangential (w) velocity components measured at $z = 2$ mm above the burner exit for NRF (case A3) is shown in Fig. 13. The mean axial velocity component is dominant by comparison with the radial and tangential velocity components in the inner flow region. The recirculation zone above the bluff body is well captured by the LDV measurement, as indicated by the negative axial velocities above that region. The shear layer location is revealed by the peak RMS velocity of the axial component. The absolute values of the mean velocity (\bar{U}) and RMS velocity (U') are calculated from the three velocity components using:

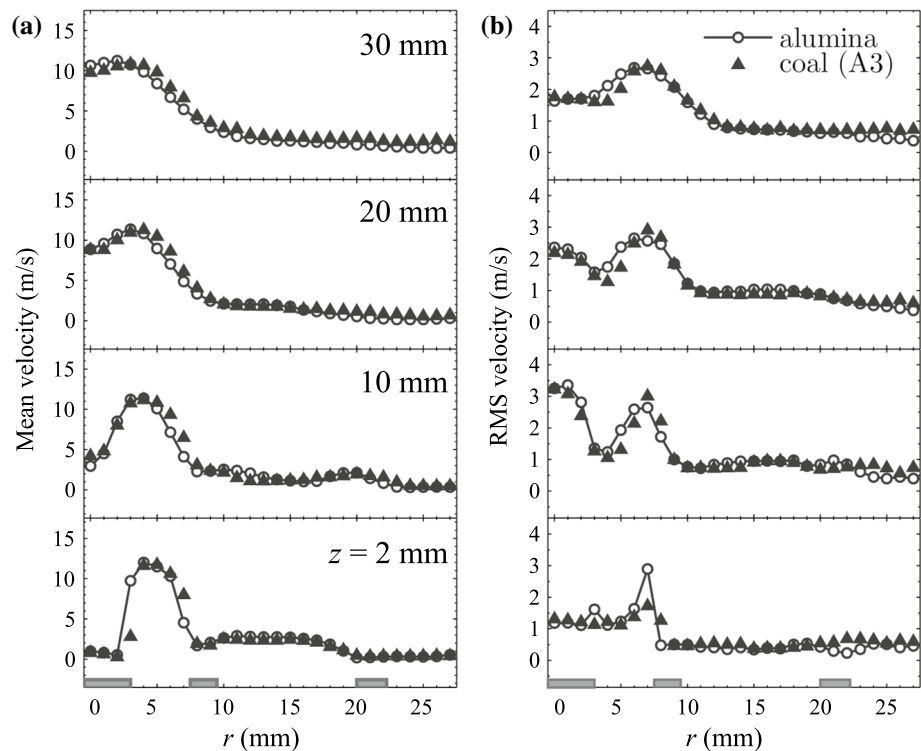
$$\bar{U} = \sqrt{\bar{u}^2 + \bar{v}^2 + \bar{w}^2} \quad (1)$$

$$U' = \sqrt{u'^2 + v'^2 + w'^2} \quad (2)$$

LDV measurements are carried out over only half of the burner due to the good axisymmetry of the flow field so as to shorten the acquisition time. The random errors introduced into the mean and RMS velocity measurements due to the finite sample size duration ($\sim 10,000$ data points per measurement location) are 1.4 and 1.8 %, respectively, for a 95 % confidence interval (Benedict and Gould 1996).

Since the cross-stream velocity values are small, in the next few plots only the absolute velocities are represented.

Fig. 14 Radial distribution of absolute velocities of alumina and coal particles (case A3) measured for non-reacting flow condition at various downstream positions ($z = 2, 10, 20$ and 30 mm). **a** Mean velocities, **b** RMS velocities



The radial distribution of the absolute velocities for gas-only and coal-laden flows under non-reacting conditions (case A3) is shown in Fig. 14. The profiles of the gas-only and coal-laden cases are largely identical, with the exception of a slight discrepancy in RMS velocities, particularly at $z = 2$ mm. This has been attributed to the larger size of the coal particles, which cannot quite follow the turbulent fluctuations (Balusamy et al. 2013). The good agreement between the velocity measurements of alumina and coal seeded flow, including the RMS velocities, indicates that most of the valid LDV signals are collected from smaller coal particles. The evolution of velocity profiles along the downstream locations indicates a broadening of the jet, which is well captured by Mie scatter measurements (Sect. 3.2).

Figure 15 shows the radial distribution of absolute mean and RMS velocities at various downstream locations for enriched air-fired cases A1 and A3, compared to the gas-only, alumina-seeded case. The mean profiles are largely similar to all three cases, but at the higher coal loadings (A3) the heat release rate creates further gas expansion, so that the velocity profiles of case A3 are wider than in the baseline case without coal. Smaller differences are apparent at the base ($z = 2$ mm), with the gas-only profile shifted outward relative to the coal-laden cases. The RMS fluctuations are clearly different between the three cases, particularly further downstream: Higher RMS fluctuations appear for the highest coal loadings. Larger particles would usually create lower RMS fluctuations if they cannot follow

the flow, but the high RMS values appear within the product region, where the particles become small or formed lighter char particles and can therefore more easily follow turbulence fluctuations. The mean velocity profiles at axial locations of 20 and 30 mm show an increase in coal particle velocities for the rich mixture (case A3) with the radial shift due to the gas expansion by the increase in flame temperature with the increase coal combustion. This is not observed for the low coal feeding rate (case A1) condition due to the lower coal devolatilization rate and subsequent burning, as evident from the low soot formation (Sect. 3.4).

Figure 16 summarizes the effect of the gas composition on the coal flame structure as well as the coal burning rate. With the replacement of N_2 by CO_2 , the flame region becomes a narrow channel, due to the absence of gas expansion, and its flame speed as well as turbulent fluctuations decrease due to the drop in coal devolatilization and burning rate.

4 Conclusions

We have successfully deployed simultaneous Mie and OH PLIF imaging techniques to investigate the structure of co-fired coal–methane piloted flames under a range of diluent and flow conditions. Additional LII measurements showed where soot particles are formed in the product zone, and pairwise two-dimensional LDV measurements showed how the velocities vary under these conditions.

Fig. 15 Radial distribution of absolute velocities of alumina (gas-only flame) and coal particles (case A1 and A3) measured for reacting flow condition at various downstream positions ($z = 2, 10, 20$ and 30 mm). **a** Mean velocities, **b** RMS velocities

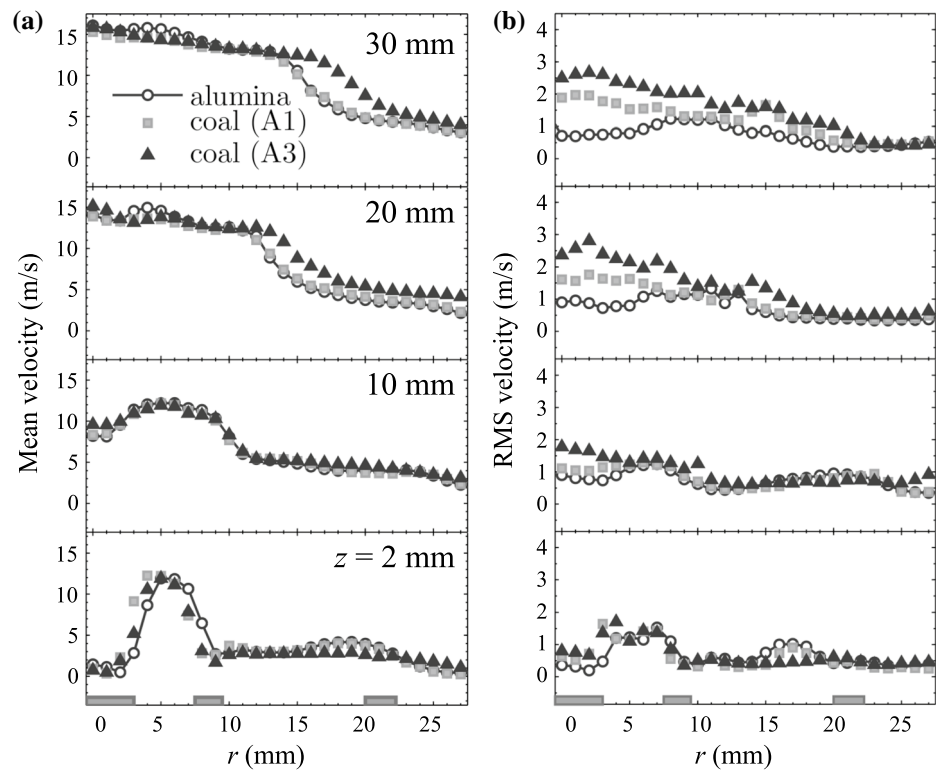
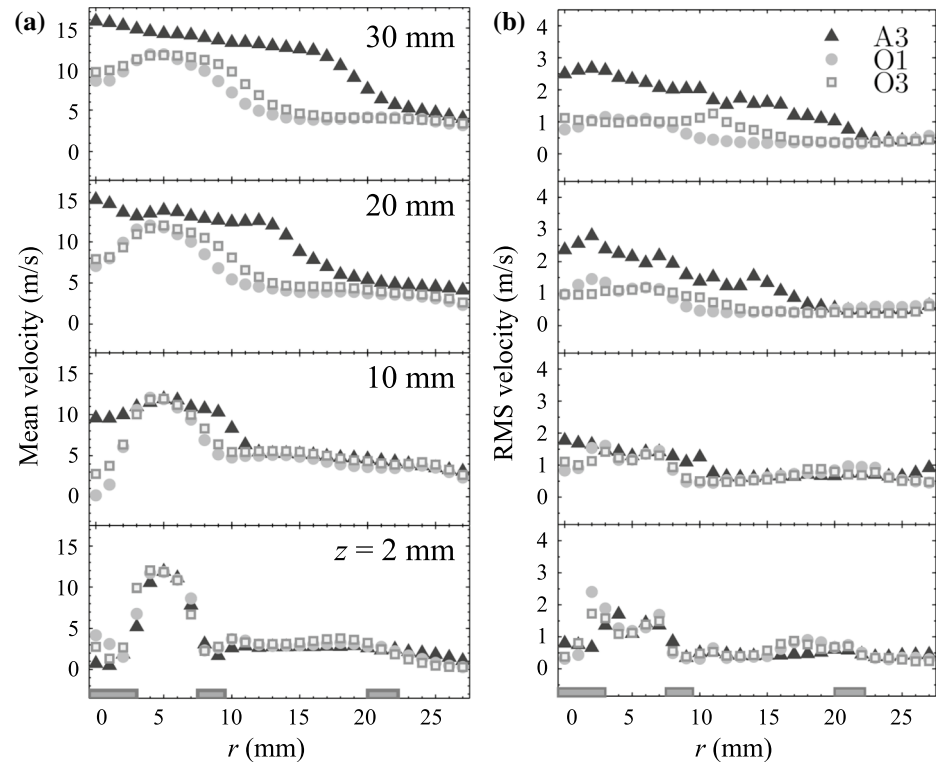


Fig. 16 Radial distribution of absolute velocities of coal particles (case A3, O1 and O3) measured for reacting flow condition at various downstream positions ($z = 2, 10, 20$ and 30 mm). **a** Mean velocities, **b** RMS velocities



The results show that a gaseous reaction zone, stabilized by the methane co-firing gas, stabilizes at the bluff body and burner lip edges. Coal particles cross this front,

ignite and devolatilize across the flame, promoting a sudden decrease in Mie scatter signal across the flame interface. At high coal particle loading rates, larger particles

survive the flame front and continue to burn downstream in luminous streaks. As the heat capacity of the diluent flows increases, product gas temperatures decrease, and the inner flame region becomes long narrow, extending beyond the field of view. As the O_2 concentration increases, product temperatures increase and the flame height decreases. High coal-loading rates lead to increased product temperatures and reaction rates, as evidenced by shorter flame zones. LII signals indicate that soot is formed in discrete regions in the wake of burning coal particles, which appear as streaky spots both in LII and in Mie scatter images. Finally, velocity measurements show the role of fuel loading and oxygen enrichment on the increased heat release rate and gas expansion, while turbulent velocity fluctuations reflect the effect of particle size changes in the overall mixture. The database generated can be obtained from the authors for validation of CFD models.

Acknowledgments The authors thank Dr. W. Nimmo for the supply of coal samples. The technical assistance of Roy Slater is gratefully acknowledged. This work is supported by EPSRC research Grant (#EP/G062153/1). Yi Gao is supported by EPSRC Grant (#EP/K02924X/1). S. Lowe acknowledges support through an EPSRC DTA grant. M. Kamal is supported by University of Engineering and Technology Peshawar (Pakistan), and Bo Tian acknowledges support from CSC.

Open Access This article is distributed under the terms of the Creative Commons Attribution 4.0 International License (<http://creativecommons.org/licenses/by/4.0/>), which permits unrestricted use, distribution, and reproduction in any medium, provided you give appropriate credit to the original author(s) and the source, provide a link to the Creative Commons license, and indicate if changes were made.

References

- Medium-Term Coal Market Report 2012 - Market Trends and Projections to 2017. ISBN 978-92-64-17795-6, International Energy Agency
- Balusamy S, Schmidt A, Hochgreb S (2013) Flow field measurements of pulverized coal combustion using optical diagnostic techniques. *Experiments in Fluids* 54(5):1–14
- Benedict LH, Gould RD (1996) Towards better uncertainty estimates for turbulence statistics. *Experiments in Fluids* 22(2):129–136
- Buhre BJP, Elliott LK, Sheng CD, Gupta RP, Wall TF (2005) Oxy-fuel combustion technology for coal-fired power generation. *Progress in Energy and Combustion Science* 31(4):283–307
- Chen L, Yong SZ, Ghoniem AF (2012) Oxy-fuel combustion of pulverized coal: Characterization, fundamentals, stabilization and CFD modeling. *Progress in Energy and Combustion Science* 38(2):156–214
- Desmira N, Nagasaka T, Narukawa K, Ishikawa A, Kitagawa K, Gupta AK (2013) Spectroscopic observation of chemical species from high-temperature air pulverized coal combustion. *Journal of Energy Resources Technology* 135(3):034,503
- Draper TS, Zeltner D, Tree DR, Xue Y, Tsiava R (2012) Two-dimensional flame temperature and emissivity measurements of pulverized oxy-coal flames. *Applied Energy* 95:38–44
- Edge P, Gharebaghi M, Irons R, Porter R, Porter R, Pourkashanian M, Smith D, Stephenson P, Williams A (2011) Combustion modelling opportunities and challenges for oxy-coal carbon capture technology. *Chemical Engineering Research and Design* 89(9):1470–1493
- Hayashi J, Hashimoto N, Nakatsuka N, Tsuji H, Watanabe H, Makino H, Akamatsu F (2013) Soot formation characteristics in a lab-scale turbulent pulverized coal flame with simultaneous planar measurements of laser induced incandescence of soot and mie scattering of pulverized coal. *Proceedings of the Combustion Institute* 34(2):2435–2443
- Hwang SM, Kurose R, Akamatsu F, Tsuji H, Makino H, Katsuki M (2005) Application of optical diagnostics techniques to a laboratory-scale turbulent pulverized coal flame. *Energy and Fuels* 19(2):382–392
- Hwang SM, Kurose R, Akamatsu F, Tsuji H, Makino H, Katsuki M (2006a) Observation of detailed structure of turbulent pulverized-coal flame by optical measurement- (part 1, time-averaged measurement of behavior of pulverized-coal particles and flame structure). *JSME International Journal Series B* 49:1316–1327
- Hwang SM, Kurose R, Akamatsu F, Tsuji H, Makino H, Katsuki M (2006b) Observation of detailed structure of turbulent pulverized-coal flame by optical measurement- (part 2, instantaneous two-dimensional measurement of combustion reaction zone and pulverized-coal particles). *JSME International Journal Series B* 49:1328–1335
- Kalt PAM, Birzer CH, Nathan GJ (2007) Corrections to facilitate planar imaging of particle concentration in particle-laden flows using mie scattering, part 1: Collimated laser sheets. *Applied Optics* 46(23):5823–5834
- Kee RJ, Rupley FM, Miller JA (1993) The chemkin thermodynamic data base. Sandia Report SAND87-8215B, UC-4
- Kihm KD, Sun F, Chigier N (1990) Laser doppler velocimetry investigation of swirler flowfields. *Journal of Propulsion and Power* 6(4):364–374
- Kurose R, Watanabe H, Makino H (2009) Numerical simulations of pulverized coal combustion. *Kona Powder Part J* 27:144–156
- McLean WJ, Hardesty DR, Pohl JH (1981) Direct observations of devolatilizing pulverized coal particles in a combustion environment. Symposium (International) on Combustion 18(1):1239–1248
- Metz B, Davidson O, de Coninck H, Loos M, Meyer L (eds) (2005) IPCC Special Report on Carbon Dioxide Capture and Storage. Cambridge University Press
- Murphy JJ, Shaddix CR (2006) Combustion kinetics of coal chars in oxygen-enriched environments. *Combustion and Flame* 144(4):710–729
- Pickett LM, Jackson RE, Tree DR (1999) Lda measurements in a pulverized coal flame at three swirl ratios. *Combustion Science and Technology* 143(1):79–107
- Prins W, Siemons R, Van Swaaij WPM, Radovanovic M (1989) Devolatilization and ignition of coal particles in a two-dimensional fluidized bed. *Combustion and Flame* 75(1):57–79
- Saito M, Sadakata M, Saka T (1987) Measurements of surface combustion rate of single coal particles in laminar flow furnace. *Combustion Science and Technology* 51(4):109–128
- Saito M, Sadakata M, Sato M, Soutome T, Murata H, Ohno Y (1991) Combustion rates of pulverized coal particles in high-temperature/high-oxygen concentration atmosphere. *Combustion and Flame* 87(1):1–12
- Shaddix CR, Molina A (2009) Particle imaging of ignition and devolatilization of pulverized coal during oxy-fuel combustion. *Proceedings of the Combustion Institute* 32(2):2091–2098
- Smith NL, Nathan GJ, Zhang DK, Nobes DS (2002) The significance of particle clustering in pulverized coal flames. *Proceedings of*

- the Combustion Institute 29(1):797–804 proceedings of the Combustion Institute
- Sung YM, Moon CE, Kim JR, Kim SC, Kim TH, Seo SI, Choi GM, Kim DJ (2011) Influence of pulverized coal properties on heat release region in turbulent jet pulverized coal flames. *Experimental Thermal and Fluid Science* 35(4):694–699
- Toftegaard MB, Brix J, Jensen PA, Glarborg P, Jensen AD (2010) Oxy-fuel combustion of solid fuels. *Progress in Energy and Combustion Science* 36(5):581–625
- Toporov D, Bocian P, Heil P, Kellermann A, Stadler H, Tschunko S, Frster M, Kneer R (2008) Detailed investigation of a pulverized fuel swirl flame in co₂/o₂ atmosphere. *Combustion and Flame* 155(4):605–618
- Wall T, Liu Y, Spero C, Elliott L, Khare S, Rathnam R, Zeenathal F, Moghtaderi B, Buhre B, Sheng C, Gupta R, Yamada T, Makino K, Yu J (2009) An overview on oxyfuel coal combustion-state of the art research and technology development. *Chemical Engineering Research and Design* 87(8):1003–1016
- Zhang L, Binner E, Qiao Y, Li CZ (2010) In situ diagnostics of victorian brown coal combustion in o₂/n₂ and o₂/co₂ mixtures in drop-tube furnace. *Fuel* 89(10):2703–2712